LA-UR- 09-00934

Approved for public release;
distribution is unlimited.

Title:	A Density-Temperature Description of the Outer Electron Radiation Belt during Geomagentic Storms
Author(s):	Michael H. Denton Joseph E. Borovsky Thomas E. Cayton
Intended for:	Journal of Geophysical Research

Los Alamos
NATIONAL LABORATORY
EST. 1943

Form 836 (7/06)

A Density-Temperature Description of the Outer Electron Radiation Belt during Geomagnetic Storms

Michael H. Denton[1], Joseph E. Borovsky[2], and Thomas E. Cayton[2].

1. Department of Communication Systems, Lancaster University, Lancaster, LA1 4WA, UK.
2. Space Science and Applications, Los Alamos National Laboratory, Los Alamos, NM 87545, USA

ABSTRACT: Electron flux measurements from 7 satellites in geosynchronous orbit from 1990-2007 are fit with relativistic bi-Maxwellians, yielding a number density n and temperature T description of the outer electron radiation belt. For 54.5 spacecraft years of measurements the median value of n is 3.7×10^{-4} cm^{-3} and the median value of T is 142 keV. General statistical properties of n, T, and the 1.1-1.5 MeV flux $\mathcal{F}$ are investigated, including local-time and solar-cycle dependencies. Using superposed-epoch analysis triggered on storm onset, the evolution of the outer electron radiation belt through high-speed-steam-driven storms is investigated. The number density decay during the calm before the storm is seen, relativistic-electron dropouts and recoveries from dropout are investigated, and the heating of the outer electron radiation belt during storms is examined. Using four different triggers (SSCs, southward-IMF CME sheaths, southward-IMF magnetic clouds, and minimum Dst), CME-driven storms are analyzed with superposed-epoch techniques. For CME-driven storms an absence of a density decay prior to storm onset is found, the compression of the outer electron radiation belt at time of SSC is analyzed, the number-density increase and temperature decrease during storm main phase is seen, and the increase in density and temperature during storm recovery phase is observed. Differences are found between the density-temperature and the flux descriptions, with more information for analysis being available in the density-temperature description.

1. Introduction

A major issue in magnetospheric physics is to understand the evolution of the radiation belts. The evolution of the outer electron radiation belt involves the addition and loss of electrons, the radial transport of electrons, and the heating and cooling of electrons. Relativistic electrons are harmful to satellite systems and instrumentation (e.g. *Wrenn* [2009]), present significant dangers to cosmonauts passing through the region, and have also been implicated as playing a limited role in the morphology of stratospheric ozone (e.g. *Winkler et al.* [2008], *Seppälä et al.* [2008]). In general, differential fluxes are used to describe the properties of the electron radiation belt and are used in studies to determine acceleration mechanisms (e.g. *Paulikas and Blake* [1979], *Nagai* [1982], *Reeves et al.* [2003], *Mann et al.* [2004], *Li et al.* [2005], *Liemohn and Chan* [2007], *Onsager et al.* [2007], *Millan and Thorne* [2007], *Summers et al.* [2007a/b], *Baker and Kanekal* [2008], *Hudson et al.* [2008], *Borovsky and Denton* [2009a]). However, fluxes are somewhat ambiguous in that increases in the flux can be caused by increases in the number of electrons or by a heating of the electrons, and likewise decreases in the flux can be caused by decreases in the number of electrons or by a cooling of the electrons.

A density and temperature description of the electron radiation belt provides substantial advantages over the flux description: changes in the number of electrons and changes in the temperature of the electrons are separated in the measurements. With slight heating or cooling of the electron population the fluxes can change by orders of magnitude; a flux description leads one to look for a particle-acceleration mechanism that can boost energies by orders of magnitude whereas a density-temperature description leads on to look for a heating mechanism that can modestly heat the electrons (cf. *Borovsky et al.* [1998c]). Hence, a density-temperature description provides a simplified and more-manageable description of the evolution of the radiation belts, with the potential to reveal physical phenomena not readily-accessible with a flux-description.

The density-temperature description of the outer electron radiation belt used that will be in this study was developed by *Cayton et al.* [1989]. In the *Cayton et al.* study, relativistic bi-Maxwellian fits of the multisatellite CPA (charged particle analyzer) measurements were used to investigate the effect of magnetospheric substorms on the outer electron radiation

belt. The study revealed that substorms result in decreases in the number density of the outer electron radiation belt at geosynchronous orbit. That study also found 27-day periodicities in the number density of the outer electron radiation belt. Four other studies have since utilised this density-temperature description of the electron radiation belt. *Borovsky et al.* [1998b] used Cayton's relativistic bi-Maxwellian fits to multisatellite SOPA (synchronous orbit particle analyzer) measurements of the outer electron radiation belt at geosynchronous orbit to study the evolution of the electron radiation belt during high-speed-stream-driven storms. *Borovsky et al.* observed that after the outer electron radiation belt was emptied of electrons at storm onset, the number density of electrons rapidly returned to a level that remained quasi-constant during the storm itself, and that increases in the relativisitic-electron flux during the storms were associated with a slow and modest heating of the outer electron radiation belt at constant density. *Borovsky and Steinberg* [2006] used Cayton's relativistic bi-Maxwellian fits to the multisatellite SOPA measurements to examine the affect of the outer plasmasphere on the outer electron radiation belt during calms periods before storms. They found that the number density of the outer electron radiation belt at geosynchronous orbit decays prior to storm onset and that the decay is stronger when the outer plasmasphere is present in the magnetosphere than when it is absent. *Borovsky and Denton* [2009c] followed up that study to quantify the number-density decay rates of the outer electron radiation belt number density during calms before storms. Finally, *Borovsky and Denton* [2009b] used Cayton's relativistic bi-Maxwellian fits to the multisatellite SOPA measurements to explore the usefulness of a specific-entropy description of the evolution of the outer electron radiation belt.

The current study presents a density-temperature overview of the evolution of the outer electron radiation belt at geosynchronous orbit during geomagnetic storms driven by high speed solar wind streams (HSSs) and driven by coronal mass ejections (CMEs). Previous work has revealed that the two types of solar wind have distinct physical consequences for the inner magnetosphere (e.g. *Wilken et al.* [1999], *Denton et al.* [2006], *Borovsky and Denton* [2006a], *Lavraud et al.,* [2006]; *Longden et al.* [2008]; *Sandanger et al.* [2009]) and more distinctions are quantified in detail in terms of electron temperature and density within the outer radiation belt. This study reveals that there is more information in a density-temperature description of the evolution of the outer electron radiation belt than there is an a flux description.

This manuscript is organized as follows. In Section 2 the relativistic bi-Maxwellian fits to energetic electrons are overviewed and the data set that will be used is described. In Section 3 the evolution of the outer electron radiation belt at geosynchronous orbit during high-speed-stream-driven storms is analysed using superposed epoch data analysis triggered by storm convection onset. In Section 4 the evolution of the outer electron radiation belt at geosynchronous orbit during coronal-mass-ejection-driven storm is analysed using superposed epoch data analysis with four separate triggers to discern the evolution during different phases of the storms. The findings of this study are summarized in Section 5.

2. Data analysis : Relativistic bi-Maxwelliean fits

The SOPA instruments [*Belian et al.,* 1992; *Cayton and Belian,* 2007] measure spin-averaged differential fluxes of energetic electrons in the energy range ~30 keV to >2 MeV at a cadence of 10 seconds. *Cayton et al.* [1989] found that the energetic-electron energy distribution functions at geosynchronous orbit could be well fit by relativistic bi-Maxwellians. For the present data analysis, the electron fluxes at geosynchronous orbit measured by SOPA instruments [*Belian et al.,* 1992] on seven Los Alamos National Laboratory (LANL) satellites (046, 095, 080, 084, 97A, 01A, and 02A) in the 18 years from 1990 through 2007 are fitted to a relativistic bi-Maxwellian distribution based on the method of *Cayton et al.* [1989] (see also *Cayton and Belian* [2007] for full details). A scatter plot of the number densities and temperatures of the two components of the bi-Maxwellian fits appears in Figure 1. The points are half-hour median values of the fit parameters for the spacecraft LANL-01a for the seven years 2001-2007. The energetic electrons at geosynchronous orbit divide into a "hard" component with a number density of ~5×10-4 cm-3 and a temperature of ~150 keV (red points in Figure 1) and a "soft" component with a number density of ~1×10-2 cm-3 and a temperature of ~300 keV (green points in Figure 1). The soft component is the suprathermal tail of the electron plasma sheet, which is associated with substorm energetic-electron injections [e.g. *Cayton et al.,* 1989; *Birn et al.,* 1998]. The hard component is the outer electron radiation belt. Note in Figure 1 that the temperature of the outer electron radiation belt (red points) varies by factors of ~2 whereas the number density varies by more than an order of magnitude.

In the first three panels of Figure 2 the number density n, temperature T, and pressure (energy density) $P=nk_BT$ of the outer electron radiation belt at geosynchronous orbit are plotted. The binning is of 955,527 half-hour medians comprising 54.5 satellite years of data from 7 satellites taken between 1990 and 2007. The top panel of Figure 2 shows the occurrence distribution of $\log_{10}(n)$. The distribution of $\log_{10}(n)$ has a modest skewness and a modest kurtosis: the distribution of n itself has a large skewness and an extraordinarily large kurtosis. The mean value of n is 4.2×10^{-4} cm^{-3} and the median value of n is 3.7×10^{-4} cm^{-3}. The number density of the outer electron radiation belt at geosynchronous orbit is about 10^{-3} times as small as the number density of the plasma sheet at geosynchronous orbit (cf. *Denton et al.* [2005]). The second panel of Figure 2 shows the occurrence distribution of the temperature T

of the electron radiation belt. The distribution of T has a slight skewness and a slight kurtosis. The mean value of T is 142 keV and the median value of T is 148 keV. Note that the relative variation of T (standard deviation divided by mean value) is about 30%; the relative variance of n is about 70%. In the third panel of Figure 2 the occurrence distribution of the pressure $P=nk_BT$ of the outer electron radiation belt at geosynchronous orbit is shown. The distribution of the pressure itself has a large skewness and a very large kurtosis. The mean value of P is 0.0104 nPa and the median value is 0.0083 nPa. In the fourth panel of Figure 2 the differential flux $\mathcal{F}$ of relativistic electrons in the 1.1-1.5 MeV energy band are binned. The binning is of 876,391 half-hour medians comprising 50.0 satellite years of data taken between 1989 and 2006. The bottom panel shows the occurrence distribution of $\log_{10}(\mathcal{F})$. The distribution of $\log_{10}(\mathcal{F})$ has a modest skewness and a modest kurtosis: the distribution of $\mathcal{F}$ itself has a large skewness and an extraordinarily large kurtosis. The mean value of $\mathcal{F}$ is 13.0 $cm^{-2}s^{-1}ster^{-1}keV^{-1}$ and the median value is 4.7 $cm^{-2}s^{-1}ster^{-1}keV^{-1}$. Note by comparing the top and bottom panels of Figure 2 that the occurrence distribution of log10(n) has a width of about 1.5 (which is 1.5 orders of magnitude of variation of n) wheras the occurrence distribution of $\log10(\mathcal{F})$ has a width of about 2.5 (which is 2.5 orders of magnitude of variation of $\mathcal{F}$). The relative variation of $\mathcal{F}$ (standard deviation divided by mean value) is about 180%, which is much larger than the relative variation of n or of T.

As measured at geosynchronous orbit, there are systematic local-time dependences in the values of the number density n and temperature T of the outer electron radiation belt. These are shown in the first two panels of Figure 3. The grey points are the half-hour measurements (with every 20th point plotted) and the red points are 3000-point running logarithmic averages of the grey points. Note that the number density (top panel) of the outer electron radiation belt at geosynchronous orbit has a weak local-time dependence with a maximum in the pre-noon sector; the temperature (bottom panel) has a similar but weaker local-time dependence. In the bottom panel of Figure 3 the relativistic-electron flux $\mathcal{F}$ at geosynchronous orbit in the 1.1-1.5 MeV energy band is plotted as a function of local time. The flux also shows the same local-time dependence as the number density n and temperature T of the electrons.

In Figure 4 the number density n (top panel), temperature T (second panel), pressure $P=nk_BT$ (third panel), and 1.1-1.5 MeV flux $\mathcal{F}$ of the outer electron radiation belt at geosynchronous orbit are plotted as a function of time for 18 years. In the top three panels the black points are 5,000-point logarithmic averages of the 955,527 half-hour measurements. Depending on the number of geosynchronous satellites in operation at the time, the 5000-point averaging represents about a 1-month running average. In the fourth panel the black points are 1440-point logarithmich averages of the 278,471 half-hour multisatellte averages of $\mathcal{F}$. Plotted in the bottom panel of Figure 4 is the international sunspot number ISN. As can be seen in the top panel of Figure 4, during years with substantial high-speed-stream activity, such as 1993-1994, 2003, and 2005 (in declining phases of the solar cycle), the number density of the outer electron radiation belt at geosynchronous orbit tends to be high. Some years of solar minimum (e.g. 1995 and 2007), the outer electron radiation belt tends to have a very low density. (This low density results in a very high specific entropy of the outer electron radiation belt during solar minimum [*Borovsky and Denton*, 2009b].) The pressure (energy content) of the outer electron radiation belt (third panel) tends to reflect these number-density trends. The solar-cycle temperature variations are less than the variations in number density, with the temperature of the outer electron radiation belt tending to be slightly higher than average during the declining phase of the solar cycle. The monthly-averaged relativistic-electron flux $\mathcal{F}$ at geosynchronous orbit also tends to reflect the trend in the number density of the outer electron radiation belt: the flux is higher during the declining phase of the solar cycle than it is during the other phases.

3. The evolution of the outer electron radiation belt during high-speed solar wind streams (HSSs)

The arrival of high speed solar wind streams (HSSs) at the Earth's magnetosphere initiates numerous physical processes including (i) a sudden onset of magnetospheric convection (cf. Figure 5), (ii) enhanced density, heating, and transport in the plasma sheet (e.g. *Borovsky et al.* [1998b], *Lavraud et al.,* [2006]; *Denton and Borovsky* [2008]), (iii) enhanced particle precipitation [*Longden et al.,* 2008], (iv) flux dropouts/recovery of outer radiation belt electrons (e.g. *Paulikas and Blake,* 1979; *O'Brien et al.,* 2001; *Borovsky and Denton,* 2009a], (v) the formation of long-lived plasmaspheric drainage plumes [*Borovsky and Denton,* 2006b, 2008] and (vi) an increase in ionospheric heating and the occurence of F-region storms [*Denton et al.,* 2009; *Sojka and McPherron,* 2009]. Many of these processes are inter-linked (e.g. *Tsurutani et al.,* [2006], *Kavanagh and Denton* [2008], *Denton et al.* [2009]). For example, the onset of convection (i) causes plasma from the outer plasmasphere to be stripped away into a plasmaspheric plume (v), which is implicated in the loss of relativistic electrons from the outer radiation belt (iv) [*Borovsky and Denton*, 2009a].

To study the behaviour of the outer electron radiation belt during high-speed-stream-driven storms we perform a superposed epoch analysis of 124 HSS storms which occured between 1993 and 2006. Previously, these events have been used successfully in studies of the magnetospheric response to HSSs [*Borovsky and Denton,* 2008, 2009a/b/c; *Denton et al.,* 2008, *Denton and Borovsky,* 2008, 2009; *Denton et al.,* 2009]. The list of HSSs was constructed based on an initial list of CIR stream interfaces for 1993-1996 provided by R. McPherron [private communication]. More events were added by searching solar wind data for years beyond 1996 and identifying typical signatures of HSSs (e.g. east-west flow deflection followed by sustained elevated solar wind speed). The final list of HSS storms between 1993 and 2006 includes an 'onset time', which is the time of storm convection onset. Convection onsets are initially detected by a strong rise in the Kp index, with the final onset time calculated to ~30 minute time resolution using changes in the MBI (Midnight Boundary Index) [*Madden and Gussenhoven,* 1990] to determine the time at which convection is equivalent to convection at a Kp value of 4^+. It should be noted that events with no discernable increase in convection following a HSS identification in the solar wind are not included in the study (see *Denton et al.* [2006] and *Denton and Borovsky* [2008] for full

details). This event selection likely corresponds to events which are Russell-McPherron effective [*Russell and McPherron,* 1973; *McPherron et al.,* 2009].

Figure 5 contains plots of a selection of superposed solar-wind, radiation belt, and geomagnetic parameters for 35 days prior to storm onset (zero epoch) and 35 days after storm onset, i.e. it encompasses more than one solar rotation period before and after the arrival of each HSS at the magnetosphere. In the top-left panel of Figure 5 the superposition of the solar-wind speed (V-SW) is show for the 124 high-speed-stream-driven storms. The dark blue curve in each panel of Figure 5 is the mean value of the data superposition. The speed is obtained from the high resolution OMNI2 database [*King and Papitashvili,* 2005]. The solar wind-speed plot indicates that at storm onset the speed is increasing and that the speed remains at an elevated level for a number of days. Typically storm onset occurs during the passage of the corotating interaction region (CIR) upstream of the high-speed wind [*Denton and Borovsky,* 2009]. The east-west component of the solar wind (VY-SW) shown in the upper-right panel of Figure 5 indicates the rapid negative-then-positive flow deflection of the CIR - the onset of the HSS-driven storm occurs within the CIR (see also Figure 1 of *Denton and Borovsky* [2008]). The superposition of the north-south (GSM) component of the interplanetary field (B_Z-GSM) for the 124 high-speed-stream-driven storms is shown in the middle-left panel of Figure 5. The superposition of B_Z indicates a strong southward turning close to storm onset. In the middle-right panel of Figure 5 the superposition of the solar-wind number density (N-SW) is plotted for the 124 high-speed-stream-driven storms. As can be seen, there is a peak in the superposed solar-wind density that is roughly concurrent with the strong southward B_Z field. The peak in density is the result of the compression of the solar wind within the CIR and the peak in solar-wind density produces a superdense plasma sheet in the magnetosphere (when the solar wind plasma is captured and heated) [*Borovsky et al.,* 1997; *Denton and Borovsky,* 2008/2009]. The geomagnetic reaction of the magnetosphere during the high-speed-stream-driven storms can be gauged in the bottom two panels of Figure 5 where superpostions of the Dst index and the Kp index are shown for the 124 events. At time t=0 there is a sharp increase in the value of Kp (storm onset) and Kp persists at elevated levels for several days after storm onset. Note in the lower-right panel of Figure 5 that prior to the increase in Kp there is a distinct period of lower-than-normal Kp in the data superposition: this is the "calm before the storm" [*Clilverd et al.,* 1993; *Borovsky and Steinberg,* 2006; *Borovsky and Denton,* 2009c]. Note also in the lower-right panel of Figure 5 the 27-day periodicity that is seen in the increase of Kp associated with the 27-day

recurrence of the high-speed streams. In the lower-left panel of Figure 5 the superposition of the Dst index is plotted for the 124 high-speed-stream-driven storms. One feature to note is the limited decrease in Dst near zero epoch. On average these high-speed-stream-driven storm events have a minimum Dst of around -30. Indeed, it is instructive to note that by simply relying on Dst as a proxy for 'storm strength', the majority of the events used in this study would likely be neglected (cf. *Denton et al.* [2006]; *Borovsky and Denton* [2006]).

Figure 6 contains epoch-time versus local-time plots of the superposed relativistic electron number density (n), temperature (T), pressure ($P=nk_BT$), and relativistic-electron flux $\mathcal{F}$ (1.1-1.5 MeV) for 124 HSSs between 1993 and 2006. The zero epoch for the superposition is again the storm-onset of magnetospheric convection. The fluxes $\mathcal{F}$ used here are the multi-satellite normalized fluxes calculated from SOPA instruments on all available spacecraft and previously used in the *Borovsky and Denton* [2009a] study. The plots in Figure 6 extend from 35-days prior to onset to 35-days after onset. Figure 6 contains a broad overview of the relativistic electron behaviour in the outer radiation belt at geosynchronous orbit during HSSs, and several features are clearly apparent. Firstly, Figure 6 shows that the density, temperature, and pressure of the outer electron radiation belt all decrease at close to zero epoch, as does the relativistic-electron flux. Secondly, Figure 6 shows that the number density, temperature, and pressure of the outer radiation belt all increase after storm onset, as does the relativistic-electron flux. Following the decrease in density/temperature around zero epoch, all four parameters are elevated for a period of ~4 days duration. This is consistent with the duration of the high-speed solar wind (upper-left panel of Figure 5), and associated elevated levels of convection (lower-right panel of Figure 5). Thirdly, Figure 6 shows that there is a pronounced quasi-27 day periodicity in all of the outer-electron-radiation-belt parameters owing to the presence of recurrent high-speed solar wind structures (cf. Figure 5).

The detailed behaviour of electrons within the outer radiation belt during a HSS-driven storm can better be grasped by examination of Figure 7. Here, the zero epoch is the onset of storm levels of convection and time extends from 5-days prior to storm onset to 5-days after storm onset. In the left-hand column of Figure 7 the superposed number density, temperature, pressure, and relativistic-electron flux (1.1-1.5 MeV) of the outer electron radiation belt at geosynchronous orbit are plotted in local-time versus time. In the right-hand column 3-hr-wide local-time cuts (23-01 LT, 05-07 LT, 11-13 LT and 17-19 LT) of the number density,

temperature, pressure, and relativistic-electron flux are plotted versus time. Each line plotted in the right-hand column is smoothed with a 10-hour box-car average in time. Four features seen in Figure 7 are discussed in the following four paragraphs and are summarised in Table 1.

Firstly, in the few days prior to storm onset there is a slow decay in the number density of the outer electron radiation belt at geosynchronous orbit whilst the temperature remains constant. This is best observed in the line plots of number density and temperature shown in Figure 7 - the number density decreases at all local times while the temperature is approximately constant at all local times. The density begins to decrease about four days prior to storm onset. Owing to this density decay, the pressure also decreases with time in the days prior to storm onset (third panels of Figure 7) and the relativistic-electron flux also decreases with time prior to the storm onset (bottom panels of Figure 7). In the days prior to the onset of HSS-driven storms, a geomagnetic calm tends to occur owing to a Russell-McPherron effect [*Borovsky and Steinberg,* 2006]. The decay of the number density of the outer electron radiation belt during these calms-prior-to-storms is attributable to the refilling of the outer plasmasphere: this refilling leads to a pitch-angle scattering of the radiation belt electrons into the atmospheric loss cone. (Note: for certain wave-particle interactions such as EMIC waves, the strength of the scattering may be dependent upon the composition of the cold plasmaspheric material.) The decay rates of the outer electron radiation belt number density prior to storm onset have been quantified by *Borovsky and Denton* [2009c].

Secondly, as shown in the top panels of Figure 7, around the time of storm onset the number density of the outer electron radiation belt suddenly decreases to very low levels (essentially to instrument-background levels). This is the well-known "relativistic-electron dropout" (e.g. *Freeman* [1964], *Nagai* [1982], *Onsager et al.* [2002], *Green et al.* [2004], *Borovsky and Denton* [2009a]) usually discussed in terms of flux observations, but here also presented in terms of electron density. Coincident with the electron density dropout is an apparent decrease in the temperature of the electrons. However, this temperature observation should be treated with caution since number-density values approach background levels during the dropout itself, making temperature calculations dubious. The relativistic-electron flux (bottom panels) also shows this relativistic-electron dropout, however the timing of the drop in the density differs slightly from the timing of the drop in flux. This is particularly noticeable in Figure 7 where the time of minimum number density (at $t \approx 0$ in the upper left

panel) is almost a half of a day sooner than the time of minimum flux (bottom-left panel). The occurrence (or not) of these relativistic-electron dropouts has been shown to be associated with the occurrence (or not) of a superdense plasma sheet in the magnetosphere during the storm [*Denton and Borovsky,* 2008; 2009]. The superdense plasma sheet has its origin in the compressed (or not) solar wind in the CIR upstream of the high-speed stream [*Denton and Borovsky,* 2009].

Thirdly, less than one day after the relativistic-electron dropout, the number density of the outer electron radiation belt at geosynchronous orbit increases sharply. This is the sudden "recovery from dropout" [*Borovsky and Denton,* 2009a], which is clearly seen in the top panels of Figure 7. Typically, but not always, the number density is higher after the recovery than it was just prior to the dropout (of course the number density had been decreasing slowly for a few days prior to the dropout proper). Also, the superposed temperature of the electrons is lower just after recovery than it was just prior to dropout (middle panels of Figure 7). The pressure (bottom panels) of the outer electron radiation belt reflects these density and temperature trends. The relativistic-electron flux (bottom panels of Figure 7) also shows this recovery from dropout. Note, however, that the recovery is more sudden when observed in number density (top-right panel) than it is when observed in relativistic-electron flux (bottom-right panel). Note also that the recovery in number density occurs earlier than does the recovery in flux. By investigating the timing of changes in the different plasma populations concerned, the recovery from dropout of the outer electron radiation belt has been associated with the termination of the superdense-plasma-sheet phase of the geomagnetic storm [*Borovsky and Denton,* 2009a].

Fourthly, Figure 7 shows that in the several days after recovery from a relativistic-electron dropout, the temperature of the outer electron radiation belt at geosynchronous orbit slowly increases with time whilst the number density remains approximately constant. This is best seen in the line plots of temperature and density in the right-hand column of Figure 7. The slow temperature increase occurs during the elevated-Kp of the several-days-long geomagnetic storm (cf. lower-right panel of Figure 5). As can be seen in the right-hand panels of Figure 7, after the rapid recovery of the number density of the outer electron radiation belt the relativistic-electron fluxes at geosynchronous orbit increase by about an order of magnitude during this extended elevated-Kp period. It is also clear in Figure 7 that this increase in the relativistic-electron fluxes by an order of magnitude occurs whilst the

temperature increases only modestly. This latter comparison highlights the dichotomy of a great particle accelerator versus a modest heater (as was noted in *Borovsky et al.* [1998]). Commensurate with this density-temperature behaviour, the pressure (thermal-energy density) of the outer electron radiation belt increases steadily for days after storm onset (Figure 7 - third panels). The heating rates of the outer electron radiation belts at geosynchronous storms (and correlated parameters) remain to be quantified.

4. The Evolution of the Outer Electron Radiation Belt during CME-Driven Storms

In contrast to recurrent high-speed-stream-driven events wherein the electron radiation belt behaviour is repeatable and easier to categorise, there are significant differences in solar-wind drivers from one magnetic-cloud event to another (cf. *Jian et al.* [2006]) making the electron radiation belt behaviour difficult to categorise. Hence, cloud-driven storms are more difficult to study via superposed-epoch analysis than are high-speed-stream-driven storms. Furthermore, complications in the interpretation of the evolution of the outer electron radiation belt during CME-driven storms arise from competing effects acting simultaneously, such as compression of the magnetosphere by solar-wind ram pressure, the distortions of the inner magnetosphere by strong ring-current-plasma perturbations (Dst effect), and the evolution of the radiation belts due to geomagnetic activity. As pointed out by *Borovsky and Denton* [2009b], a typical (but not unique) temporal sequence for the solar-wind driver is interplanetary-shock arrival, passage of the CME sheath, and passage of the southward-IMF portion of the cloud. The shock may or may not be present, the sheath may or may not drive the magnetosphere, and the cloud may or may not have a southward-IMF portion. In addition, there may or may not be a northward-IMF portion of the cloud between the sheath and the southward-IMF portion of the cloud.

For cloud-driven storms, a standard trigger to take for the zero epoch of the data superposition is the minimum value of the Dst index for the storm (e.g. *Denton et al.* [2005, 2006], *Zhang et al.* [2006]). Note however, taking a single trigger at Dst minimum to analyse CME-driven storms is a method that mixes several cloud-driven storm phases together owing to the storm-to-storm differences in the sequences and to the differing temporal durations of the phases. Such a single-trigger superposition of measurements from 78 CME-driven storms appears in Figure 8, with the zero epoch taken to be the time of minimum Dst. The 78 storms are the CME-driven events utilised in the superposed epoch study of the magnetospheric hot plasmas by *Denton et al.* [2006]. In the top panel of Figure 8 the superposition of the number density of the outer electron radiation belt at geosynchronous orbit is plotted, in the second panel the superposition of the temperature is plotted, in the third panel the superposition of the pressure $P=nk_BT$ is plotted, in the fourth panel the superposition of the 1.1-1.5 MeV relativistic-electron flux is plotted, and in the bottom the panel the superposition of the Dst

index is plotted. The Dst plot indicates the main phase of the storm (Dst decreasing) and the recovery phase of the storm (Dst increasing back to quiet levels). As seen in the top panel of Figure 8, the general trend for the number density of the outer electron radiation belt at geosynchronous orbit is a density drop during the main phase of the storm just prior to the time of minimum Dst and then a large density increase during the early part of the recovery phase after minimum Dst followed by a density decrease later in the recovery phase. Note that unlike the case of high-speed-stream-driven storms (e.g. Figure 7), there is not a decrease of the number density of the outer electron radiation belt at geosynchronous orbit in the several days prior to storm onset (i.e. there is no appreciable calm-before-the-storm effect in the superposed-epoch data for CME-driven storms). The general trend of the temperature of the outer electron radiation belt at geosynchronous orbit (second panel of Figure 8) is much simpler: a temperature decrease during the main phase and a temperature recovery during the recovery phase. The trend in the pressure of the outer electron radiation belt (third panel in Figure 8) follows the trend in the number density: a decrease in the pressure during the main phase and an increase and then decrease in the pressure during the recovery phase. The trend of the relativistic-electron flux during CME-driven storms (bottom panel of Figure 8) is more like the simple trend in the outer-electron-radiation-belt temperature than the complicated trend in the density: the relativistic-electron flux exhibits a decrease during the main phase of the storm followed by an increase during the recovery phase. Note that the temporal width of the decrease in the relativistic-electron flux (fourth panel) is much greater than the temporal width of the decrease in number density (top panel). The width of the relativistic-electron flux signal is similar to the width of the temperature signal (second panel). Note also that in the superposed averages the relativistic-electron flux after the CME-driven storms is approximately the same as the relativistic-electron flux before the storms.

In the remainder of this section, four different zero-epochs (triggers) for the data superpositions are used to piecewise analyse the evolution of cloud-driven storms. All interpretation of the superposed data is restricted to the temporal vicinity of the trigger. The four zero-epochs used below are: (i) trigger on the arrival of the interplanetary shock, (ii) trigger on the beginning of sheath, (iii) trigger on the beginning of southward-IMF portion of cloud, and (iv) trigger on the end of southward-IMF portion of cloud. The results of this analysis are summarised in Table 2.

First the reaction of the outer electron radiation belt at geosynchronous orbit to the arrival of the interplanetary shock and compressed CME-sheath plasma is examined. In the data superposition shown in Figure 9 the zero epoch is taken to be the stormtime sudden commencement (SSC) at Earth, obtained from a collection 535 well-formed SSC events from the NOAA National Geophysical Data Center SSC list. Figure 9 contains plots of the superposed averages of the outer electron radiation belt number density n (top-panel), temperature T (second-panel), pressure P (middle-panel), and 1.1-1.5 MeV electron flux (fourth panel) at geosynchronous orbit. The superposition of the Dst index for these events is also shown (bottom panel); here the sharp positive increase in Dst associated with the shock arrival at Earth at t=0 is seen. As can be seen in the first three panels of Figure 9, the arrival of the interplanetary shock at t = 0 results in sudden strong decreases in the number density and the pressure of the outer electron radiation belt, with a slight decrease in the temperature commencing at time of SSC. In the fourth panel it is seen that the relativistic-electron flux $\mathcal{F}$ also makes a sudden strong decrease. These reactions are noted in Table 2. Note that the fractional decrease in the flux near t=0 is much smaller than the fractional decrease in the number density: comparing the values at time t = +2 hr with the values at time t = -1 hr the flux $\mathcal{F}$ decreases to 70% of its initial value whilst the number density n decreases to 42% of its initial value. The density decrease at geosynchronous orbit at time t = 0 is probably owed to a rapid compression of the magnetosphere by the increase in solar-wind ram pressure (higher velocity and higher density) behind the interplanetary shock, bringing more-tenuous outer-magnetospheric regions to geosynchronous orbit. After the shock passage at time t=0, the Earth's magnetosphere is within the compressed magnetosheath plasma ahead of the coronal mass ejection. Depending on the orientation of the IMF in this sheath plasma, from event to event the sheath may or may not drive geomagnetic activity in the Earth's magnetosphere. The steady decrease in the value of Dst immediately after t=0 in the superposition of the Dst index for these SSC events (bottom panel of Figure 9) indicates that there is some driving by the sheath.

In Figure 10 set of 16 CME-driven storm events wherein the IMF of the sheath plasma is distinctly southward is examined. Figure 10 contains plots of the superpositions of the outer electron radiation belt number density n (top-panel), temperature T (second-panel), pressure P (middle-panel), and 1.1-1.5 MeV electron flux (fourth panel) at geosynchronous orbit. The superposition of the Kp index for these events is also shown (bottom panel). Time t=0 is

taken to be the onset of the southward IMF (GSM) at Earth in the sheath plasma; the sudden increase in Kp near t=0 indicates the onset of driving by the sheath plasmas; note that the Kp index has a 3-hr resolution, so the increase begins approximately 3 hrs prior to t=0. The temporal profiles of the number density, the temperature, the pressure, and the relativistic-electron flux are all very similar to the profiles in Figure 9 where t=0 was the SSC (arrival of the interplanetary shock). This similarity may indicate that the reaction of the outer electron radiation belt at geosynchronous orbit is dominated by the compression of the magnetosphere..

To study the reaction of the outer electron radiation belt at geosynchronous orbit when the magnetosphere is driven (strongly) by the southward-IMF of a magnetic cloud, a subset of 13 well-defined magnetic clouds with southward-IMF (GSM) portions was extracted from the set of Dst storms that was used in the study by *Denton et al.* [2005]. These magnetic clouds were identified using SWEPAM plasma and electron measurements [*McComas et al.,* 1998] and MAG magnetic-field measurements [*Smith et al.,* 1998] onboard the ACE satellite upstream of the Earth. The clouds in the solar wind were identified by having a well ordered magnetic field, low solar-wind ion temperatures, and bi-directional electron heat flux. In Figure 11 a superposition of the measurements of the outer electron radiation belt at geosynchronous orbit is created by triggering the zero epoch on the onset of the southward-IMF portions of those 13 magnetic clouds. Figure 11 contains plots of the superposed averages of the outer electron radiation belt number density n (top-panel), temperature T (second-panel), pressure P (middle-panel), and 1.1-1.5 MeV electron flux (fourth panel) at geosynchronous orbit. The superposition of the Kp index for these events is also shown (bottom panel). Note that immediately prior to the southward-IMF portions of clouds there can be (a) sheath plasma (which may or may not drive geomagnetic activity) or (b) northward-IMF magnetic cloud (which will not drive geomagnetic activity). As can be seen in the bottom panel of Figure 11, Kp was elevated prior to t=0 in the superposition indicating that there was driving before t=0 in some of the events. As can be seen in the first and third panels of Figure 11, the number density and the pressure begin to increase when the southward-IMF portion of the cloud arrives. This increase with time during the southward IMF of the cloud is associated with the strong geomagnetic activity in the Earth's magnetosphere, as shown in the bottom panel. As can be seen in the second panel of Figure 11, the temperature of the outer electron radiation belt at geosynchronous orbit, which was decreasing with time before the arrival of the southward-IMF portion of the cloud, continues

to decrease during the southward-IMF portion of the cloud. Note that, at time t=0 in Figure 11, the number density n of the outer electron radiation belt is quite low (~1×10^{-4} cm^{-3}) and the temperature is quite low (~100 keV). The temporal evolution of the relativistic-electron flux (fourth panel in Figure 11) differs from the behaviour of the number density and the temperature: the relativistic-electron flux holds constant while the density increases and the temperature decreases.

In Figure 12 the properties of the outer electron radiation belt at geosynchronous orbit are shown triggered on the minimum value of Dst for CME-driven storms. 17 cloud-driven storms with large, single-dip, negative-Dst perturbations were selected from the list of Dst storms first used in *Denton et al.* [2006]. Triggering on the minimum value of Dst (by definition the end of the storm main phase and beginning of the storm recovery phase) likely represents the end of strong southward-IMF driving of the cloud-driven storm. Figure 12 contains plots of the superposed averages of the outer electron radiation belt number density n (top-panel), temperature T (second-panel), pressure P (middle-panel), and 1.1-1.5 MeV electron flux $\mathcal{F}$ (fourth panel) at geosynchronous orbit. The superposition of the Dst index for these events is also shown (bottom panel). In the top panel of Figure 12 the number density of the outer electron radiation belt is seen to increase steadily with time as Dst recovers. In the second panel the temperature of the outer electron radiation belt at geosynchronous orbit shows a steady slow increase as Dst recovers. In the third panel the pressure of the outer electron radiation belt at geosynchronous orbit shows a steady increase throughout the recovery phase, tracking the evolution of the number density. The relativistic-electron flux (fourth panel in Figure 12) shows the same trend as the number density and temperature; a steady increase with time as Dst recovers. These changes are noted in Table 2. The temporal profile of the relativistic-electron flux is more similar to that of the temperature than to that of the number density. The evolution of the temperature and number density of the outer electron radiation belt at geosynchronous orbit around the minimum-Dst time may be governed by a combination of the cessation of geomagnetic activity and the inflation and deflation of the dipole magnetic field owing to the "Dst effect" [e.g. *Dessler and Karplus,* 1961; *Kim and Chan,* 1997].

5. Summary

Analysis of almost one million individual bi-Maxwellian fits to relativistic electron flux data has been performed. The findings of the study are summarized below. The analysis demonstrates the strength of a density-temperature description of the outer electron radiation belt.

5.A The General Properties of the Outer Electron Radiation Belt

In Section 3 the outer electron radiation belt at geosynchronous orbit is statistically analyzed. The findings of that statistical analysis are the following.

1. At geosynchronous orbit, the median values of the number density is $n = 3.7\times10^{-4}$ cm^{-3}, the median value of the temperature is T = 142 keV, and the median value of the 1.1-1.5 MeV electron flux $\mathcal{F}$ is 4.7 $cm^{-2}s^{-1}ster^{-1}keV^{-1}$. The median value of the pressure $P = nk_BT$ is 8.3×10^{-3} nPa.

2. The fractional variations of the number density n and the temperature T are less than the fractional variations in the relativistic-electron flux $\mathcal{F}$.

3. The density, temperature, and relativistic-electron flux all show similar local-time dependences with peaks in all three quantities near local noon and minima in the quantities near local midnight. The local-time variation of the temperature is weaker than the local-time variations in n and $\mathcal{F}$.

4. There are systematic solar-cycle dependencies to n, T, and $\mathcal{F}$. The number density n and temperature T are higher during the declining phase than during the other phases of the solar cycle. The relativistic-electron flux $\mathcal{F}$ reflects these n an T trends.

5.B Evolution during High-Speed-Stream-Driven Storms

In Section 4, superposed-epoch analysis was used to study the evolution of the outer electron radiation belt at geosynchronous orbit during high-speed-steam-driven storms. The findings of that investigation are the following.

1. Associated with high-speed-steam-driven storms, there are clear 27-day periodicities in the number density n, temperature T, and relativistic-electron flux $\mathcal{F}$ of the outer electron radiation belt at geosynchronous orbit.

2. For several days prior to high-speed-steam-driven storms, the number density n of the outer electron radiation belt decreases slowly while the temperature T remains approximately constant. The relativistic-electron flux $\mathcal{F}$ also decreases slowly during this period. The decrease in n is attributable to the build up of the outer plasmasphere during calms before storms. The decrease in $\mathcal{F}$ is attributable to the decrease in n.

3. Near the onset time of a high-speed-steam-driven storm there is a sudden drop in the number density n of the outer electron radiation belt at geosynchronous orbit. The relativistic-electron flux $\mathcal{F}$ also decreases suddenly, but the flux drop is later in time than the number-density drop. This sudden decrease is the well known "relativistic-electron dropout" of high-speed-steam-driven storms.

4. Less than one day after its sudden drop, the number density n of the outer electron radiation belt shows a sudden increase (the "recovery from dropout"). The relativistic-electron flux $\mathcal{F}$ also shows this sudden recovery from dropout, but its recovery is weaker and later in time than the number-density recovery.

5. After the recovery from dropout, the temperature T of the outer electron radiation belt at geosynchronous orbit slowly increases with time during the several days of the high-speed-steam-driven storm while the number density is approximately constant. During this time interval the relativistic-electron flux $\mathcal{F}$ steadily increases as the temperature increases at constant density. This steady increase in the relativistic-electron flux during the storm is attributable to a steady heating of the outer electron radiation belt.

6. The number density n of the outer electron radiation belt at geosynchronous orbit tends to be higher after a storm than it was before the storm. The temperature T of the outer electron radiation belt tends to be about the same after a storm as before. The relativistic-electron flux $\mathcal{F}$ tends to be higher after a storm than before the storm.

5.C Evolution during CME-driven Storms

In Section 5, superposed-epoch analysis with multiple trigger selections was used to study the evolution of the outer electron radiation belt at geosynchronous orbit during CME storms. The findings of that investigation are the following.

1. Unlike the case for high-speed-steam-driven storms, there tends to be no systematic temporal decrease in the number density n or relativistic-electron flux $\mathcal{F}$ of the outer electron radiation belt at geosynchronous orbit in the days prior to the onset of CME-driven storms. This lacking is probably associated with the lack of a systematic calm before CME-driven storms.

2. When the storm sudden commencement (SSC) occurs (arrival of interplanetary shock at Earth), the number density n and the relativistic-electron flux $\mathcal{F}$ of the outer electron radiation belt at geosynchronous orbit decrease suddenly. The fractional decrease in the number density is larger than the fractional decrease in the relativistic-electron flux. The temperature decrease at the time of SSC is very slight. The sudden density decrease is attributable to a sudden compression of the magnetosphere delivering higher-L energetic electrons to geosynchronous orbit.

3. During the southward-IMF (GSM) portions of magnetic clouds (storm main phase), the number density n of the outer electron radiation belt at geosynchronous orbit increases with time while the temperature T decreases with time. The relativistic-electron flux $\mathcal{F}$ remains approximately constant during the southward-IMF portions of the magnetic clouds.

4. During the recovery phase of CME-driven storms (the interval wherein Dst increases toward quiet-time values after the time of minimum Dst) the number density n of the outer

electron radiation belt at geosynchronous orbit increases and the temperature T increases. During the recovery phase the relativistic-electron flux $\mathcal{F}$ also increases, mimicking the temporal profile of the temperature more than the temporal profile of the number density.

5. The number density n, temperature T, and relativistic-electron flux $\mathcal{F}$ of the outer electron radiation belt at geosynchronous orbit all tend to have the same values after a CME-driven storm as they did before the storm.

Acknowledgements

The authors would like to thank the Space Physics Data Facility (SPDF) and National Space Science Data Center (NSSDC) for provision of the OMNI2 database, World Data Centre C1 at Rutherford-Appleton Laboratory in the UK for provision of the geomagnetic indices used in this study, and Bob McPherron for providing an updated list of stream interfaces. We also thank the U.S. Air Force Research Laboratory, Hanscom Air Force Base, Mass. for providing the Midnight Boundary Index. We thank Reiner Friedel for graciously running the relativisitic fits to the original SOPA data, and thank Michelle Thomsen for helpful comments. This work was supported by the NASA Living with a Star TR&T Program and by the Los Alamos National Laboratory LDRD Program. Parts of this work were carried out at Los Alamos National Laboratory during summer 2008 and MHD wishes to thank ISR-1 and particularly JEB for financial support and hospitality during this visit.

References

Baker, D. N., and S. G. Kanekal, Solar cycle changes, geomagnetic variations, and energetic particle properties in the inner magnetosphere, J. Atmos. Sol-Terr. Phys., 70, 195-206, 2008.

Belian, R. D., G. R. Gisler, T. Cayton, and R. Christensen, High-Z energetic particles at geostationary orbit during the great proton event seriew of October 1989, J. Geophys. Res., 97, 16897-16906, 1992.

Birn, J., M. F. Thomsen, J. E. Borovsky, G. D. Reeves, D. J. McComas, R. D. Belian, and M. Hesse, Substorm electron injections: Geosynchronous observations and test particle simulations, J. Geophys. Res., 103, 9235-9248, 1998.

Borovsky, J. E., and M. H. Denton, Electron loss rates from the outer radiation belt caused by filling of the outer plasmasphere: The calm before the storm, J. Geophys. Res., submitted, 2009c.

Borovsky, J. E., and M. H. Denton, Examining the specific entropy (density of adiabatic invariants) of the outer electron radiation belt, J. Geophys. Res., submitted, 2009b.

Borovsky, J. E., and M. H. Denton, Relativistic electron dropouts and recovery: a superposed-epoch study of the magnetosphere and the solar wind, J. Geophys. Res., (in press), 2009a.

Borovsky, J. E., and M. H. Denton, A statistical look at plasmaspheric drainage plumes, J. Geophys. Res., 113, A09221, doi:10.1029/2007JA012994, 2008.

Borovsky, J. E., and M. H. Denton, Differences between CME-driven storms and CIR-driven storms, J. Geophys. Res., 111, A07S08, doi.10.1029/2005JA011447, 2006a.

Borovsky, J. E., and M. H. Denton, Effect of plasmaspheric drainage plumes on solar-wind/magnetosphere coupling, Geophys. Res. Lett., 33, L20101, doi:10.1029/2006GL026519, 2006b.

Borovsky, J. E., and J. T. Steinberg, The "calm before the storm" in CIR/magnetosphere interactions: occurrence statistics, solar wind statistics, and magnetospheric preconditioning, J. Geophys. Res., 111, A07S10, doi:10.1029/2005JA011447, 2006.

Borovsky, J. E., M. Hesse, J. Birn, and M. M. Kuznetsova, What determines the reconnection rate at the dayside magnetosphere?, submitted to J. Geophys. Res., 2007.

Borovsky, J. E., M. F. Thomsen and R. C. Elphic, The driving of the plasma sheet by the solar wind, J. Geophys. Res., 103, 17,617-17,639, 1998a.

Borovsky, J. E., M. F. Thomsen, R. C. Elphic, T. E. Cayton and D. J. McComas, The transport of plasma sheet material from the distant tail to geosynchronous orbit, J. Geophys. Res., 103, 20,297-20,331, 1998b.

Borovsky, J. E., M. F. Thomsen, D. J. McComas, T. E. Cayton, and D. J. Knipp, Magnetospheric dynamics and mass flow during the November-1993 storm, J. Geophys. Res., 103, 26, 26373-26394, 1998c.

Borovsky, J. E, M. F. Thomsen and D. J. McComas, The superdense plasma sheet: plasmaspheric origin, solar wind origin or ionospheric origin?, J. Geophys. Res., 102, 22,089, 1997.

Brace, L. H., E. J. Maier, J. H. Hoffman, J. Whitteker, G. G. Shepherd, Deformation of the nightside plasmasphere and ionosphere during the August 1972 geomagnetic storm, J. Geophys. Res., 79, 5211-5218, 1974.

Cane, H. V., and I. V. Richardson, Interplanetary coronal mass ejections in the near-Earth solar wind during 1996-2002, J. Geophys. Res., 108, 1156, doi:10.1029/2002JA009817, 2003.

Cayton, T. E., R. D. Belian, S. P. Gary, T. A. Fritz, and D. N. Baker, Energetic electron components at geosynchronous orbit, Geophys. Res. Lett., 16, 2, 147-150, 1989.

Cayton, T. E., and R. D. Belian, Numerical modeling of the synchronous orbit particle analyser (SOPA, Version 2) that flew on S/C 1990-095, LA Rep. LA-14335, Los Alamos Natl. Lab., Los Alamos, NM 87545, 2007.

Chappell, C. R., K. K. Harris, and G. W. Sharp, The morphology of the bulge region of the plasmasphere, J. Geophys. Res., 75, 3848, 1970.

Clilverd, M. A., T. D. G. Clark, A. J. Smith, and N. R. Thomson, Observation of a decrease in mid-latitude whistler mode signal occurrence prior to geomagnetic storms, J. Atmos. Terr. Phys., 55, 10, 1479-1485, 1993.

Denton, M. H., J. E. Borovsky, R. B. Horne, R. L. McPherron, S. K. Morley, and B. T. Tsurutani., Introduction to special issue on high speed solar wind streams and geospace interactions, J. Atmos. Sol-Terr. Phys., (in press), 2009.

Denton, M. H., T. Ulich, and E. Turunen, Modification of mid-latitude ionospheric parameters in the F2 layer by persistent high speed solar wind streams, Space Weather, (in press) 2009.

Denton, M. H., and J. E. Borovsky, The superdense plasma sheet in the magnetosphere during high-speed-stream-driven storms: plasma transport and timesclaes, J. Atmos. Sol-Terr. Phys., in press, 2009

Denton, M. H., and J. E. Borovsky, Superposed epoch analysis of high-speed-stream effects at geosynchronous orbit: hot plasma, cold plasma, and the solar wind, J. Geophys. Res., 113, A07216, doi:10.1029/2007JA012998, 2008.

Denton, M. H., M. F. Thomsen, B. Lavraud, M. G. Henderson, R. M. Skoug, H. O. Funsten, J.-M. Jahn, C. J. Pollock and J. M. Weygand, Transport of plasma sheet material to the inner magnetosphere, Geophys. Res. Lett., 34, L04105, doi:10.1029/2006GL027886, 2007.

Denton, M. H., J. E. Borovsky, R. M. Skoug, M. F. Thomsen, B. Lavraud, M. G. Henderson, R. L. McPherron, J. C. Zhang, and M. W. Liemohn, Geomagnetic storms driven by ICME- and CIR-dominated solar wind, J. Geophys. Res., 111, A07S07, doi:10.1029/2005JA011436, 2006.

Denton, M. H., M. F. Thomsen, H. Korth, S. Lynch, J. C. Zhang, and M. W. Liemohn, Bulk plasma properties at geosynchronous orbit, J. Geophys. Res., 110, A07223, doi:10.1029/2004JA010861, 2005.

Denton, M. H., G. J .Bailey, C. R. Wilford, A. S .Rodger, and S. Venkatraman, He+ dominance in the plasmasphere during geomagnetically disturbed periods: 1. Observational results, Ann. Geophys., 20, 461-470, 2002.

Elphic, R. C., M. F. Thomsen, J. E. Borovsky, and D. E. McComas, Inner edge of the electron plasma sheet: Empirical models of boundary location, J. Geophys. Res., 104, 22,679-22693, 1999.

Freeman, J. W., The morphology of the electron distribution in the outer radiation zone and near the magnetospheric boundary as observed by Explorer 12, J. Geophys. Res., 69, 1691-1723, 1964.

Goldstein, J., and B. R. Sandel., The global pattern of evolution of plasmaspheric drainage plumes, In: Inner Magnetosphere Interactions: New Perspectives from Imaging, Geophysical Monograph Series 159, AGU, 2005.

Gonzalez, W. D., J. A. Joselyn, Y. Kamide, H. W. Kroehl, G. Rostoker, B. T. Tsurutani and V. M. Vasyliunas, What is a geomagnetic storm?, J. Geophys. Res., 99, 5,771-5,792, 1994.

Grebowsky, J. M., Model study of plasmapause motion, J. Geophys. Res., 75, 4329-4333, 1970.

Green, J. C., T. G. Onsager, T. P. O'Brien, and D. N. Baker, Testing loss mechanisms capable of rapidly depleting relativistic electron flux in the Earth's outer radiation belt, J. Geophys. Res., 109, A12211, 2004.

Higel, B., and W. Lei, Electron density and plasmapause characteristics at 6.6 RE: A statistical study of GEOS 2 relaxation sounder data, J. Geophys. Res., 89, 1583, 1984.

Hudson, M. K., B. T. Kress, H-R. Mueller, J. A. Zastrow, and J. B. Blake, Relationship of the Van Allen radiation belts to solar wind drivers, J. Atmos. Sol-Terr. Phys., 70, 708-729, 2008.

Iles, R. H. A., A. N. Fazakerley, A. D. Johnstone, N. P. Meredith, and P. Bühler, The relativistic electron response in the outer radiation belt during magnetic storms, Ann. Geophys., 20, 957-965, 2002.

Kavanagh, A., and M. H. Denton, High-speed solar wind streams and geospace interactions, Astron. Geophys., 48, 6.24-6.26, 2007.

King, J. H., and N. E. Papitashvili, Solar wind spatial scales in and comparisons of hourly Wind and ACE plasma and magnetic field data, J. Geophys. Res., 110, A02104, doi:10.1029/2004JA010649, 2005.

Kersley, L., and J. A. Klobuchar, Storm associated protonospheric depletion and recovery, Planet. Space Sci., 28, 453-458, 1980.

Lavraud, B., M. F. Thomsen, J. E. Borovsky, M. H. Denton, and T. I. Pulkkinen, Magnetosphere preconditioning under northward IMF: Evidence from the study of coronal mass ejection and corotating interaction region geoeffectiveness, J. Geophys. Res., 111, A09208, doi:10.1029/2005JA011566, 2006.

Lavraud, B., M. H. Denton, M. F. Thomsen, J. E. Borovsky and R. H. W. Friedel, Superposed epoch analysis of dense plasma access to geosynchronous orbit, Ann. Geophys., 23, 2519-2529, SRef-ID: 1432-0576/ag/2005-23-2519, 2005.

Li, X., D. N. Baker, M. Temerin, G. Reeves, R. Friedel, and C. Shen, Energetic electrons, 50 keV to 6 MeV, at geosynchronous orbit: Their responses to solar wind variations, Space Weather, 3, S04001, doi:10.1029/2004SW000105, 2005.

Liemohn, M. W., and A. A. Chan, Unravelling the causes of radiation belt enhancements, EOS Trans., AGU, Vol. 88, No. 42, 2007.

Lindsay, G. M., C. T. Russell, and J. G. Luhmann, Coronal mass ejections and stream interaction region characteristics and their potential geomagnetic consequences, J. Geophys. Res., 100, 16999-17013, 1995.

Longden, N., M. H. Denton and F. Honary, Particle precipitation during ICME-driven and CIR-driven geomagnetic storms, J. Geophys. Res., 113, A06205, doi:10.1029/2007JA012752, 2008.

MacDonald, E. A., M. H. Denton, M. F. Thomsen and S. P. Gary, Superposed epoch analysis of a whistler instability criterion at geosynchronous orbit during geomagnetic storms, J. Atmos. Sol-Terr. Phys., 70, 1789-1796, 2008.

McPherron, R. L., D. N. Baker, and N. U. Crooker, Role of the Russell-McPherron effect in the acceleration of relativistic electrons, J. Atmos. Sol-Terr. Phys., (in press), 2008.

McPherron, R. L., and J. Weygand, The solar wind and geomagnetic activity as a function of time relative to corotating interaction regions, in Recurrent Geomagnetic Storms: Corotating Solar Wind Streams, edited by B. T. Tsurutani, R. L. McPherron, W. D. Gonzalez, G. Lu, J. H. A. Sobral and N. Gopalswamy, pg. 125, AGU, 2006;

Madden, D., and M. S. Gussenhoven, Auroral Boundary Index from 1983 to 1990, Tech Report GL-TR-90-0358, Air Force Geophysics Laboratory, Hanscom AFB, MA, 21 Dec. 1990.

Mann, I. R., T. P. O'Brien, and D. K. Milling, Correlations between ULF wave power, solar wind speed, and relativistic electron flux in the magnetosphere: Solar cycle dependence, J. Atmos. Sol-Terr. Phys., 66, 187-198, 2004.

Meredith, N. P., R. B. Horne, R. M. Thorne, D. Summers, and R. A. Anderson, Substorm dependence of plasmaspheric hiss, J. Geophys. Res., 109, A06209, doi:10.1029/2004JA010387, 2004.

Millan, R. M., and R. M. Thorne, Review of radiation belt relativistic electron losses, J. Atmos. Sol-Terr. Phys., 69, 362-377, 2007.

Nagai, T., Local time dependence of electron flux changes during substorms derived from multi-satellite observations at geosynchronous orbit, J. Geophys. Res., 87, 3456-3468, 1982.

O'Brien, T. P., and C. L. Lemon, Reanalysis of plasma measurements at geosynchronous orbit, Space Weather, 5, S03007, doi:10.1029/2006SW000279, 2007.

O'Brien, T. P., R. L. McPherron, D. Sornette, G. D. Reeves, R. Friedel, and H. J. Singer, Which magnetic storms produce relativistic electrons at geosynchronous orbit, J. Geophys. Res., 106, 15533-15544, 2001.

Onsager, T. G., J. C. Green, G. D. Reeves, and H. J. Singer, Solar wind and magnetospheric conditions leading to the abrupt loss of outer radiation belt electrons, J. Geophys. Res., 112, A01202, doi:10.1029/2006JA01178, 2007.

Onsager, T. G., G. Rostoker, H.-J. Kim, G. D. Reeves, T. Obara, H. J. Singer, and C. Smithtro, Radiation belt electron flux dropouts: Local time, radial, and particle-energy dependence, J. Geophys. Res., 107, 1382, 2002.

Paulikas, G. A., and J. B. Blake, Effects of the solar wind on magnetospheric dynamics: Energetic electrons at the synchronous orbit, Quantitative Modeling of Magnetospheric Processes, Geophys. Monogr. Ser., vol. 21, edited by W. P. Olsen, p. 180, AGU, Washington, D.C., 1979.

Reeves, G. D., K. L. McAdams, R. H. W. Friedel, and T. P. O'Brien, Acceleration and loss of relativistic electrons during geomagnetic storms, Geophys. Res. Lett., 30, 1529-1532, doi:10.1029/2002GL016513, 2003.

Rodger, C. J., T. Raita, M. A. Clilverd, A. Seppälä, S. Dietrich, N. R. Thomsen, and T. Ulich, Observations of relativistic electron precipitation from the radiation belts driven by EMIC waves, Geophys. Res. Lett., doi:10.1029/2008GL034804, (in press), 2008.

Russell, C. T., and R. L. McPherron, Semiannual variation of geomagnetic activity, J. Geophys. Res., 78, 92-108, 1973.

Sandanger, M. I. J., F. Søraas, M. Sørbø, K. Aarsnes, K. Oksavik, and D. S. Evans, Relativistic electron losses related to EMIC waves during CIR and CME storms, J. Atmos. Sol-Terr. Phys., doi:10.1016/j.jastp.2008.07.006, (in press), 2009.

Spiro, R. W., M. Harel, R. A. Wolf and P. H. Reiff, Quantitative simulation of a magnetospheric substorm. 3. Plasmaspheric electric fields and evolution of the plasmapause, J. Geophys. Res., 86, 2261-2272, 1981.

Summers, D., N. Binbin, and N. P. Meredith, Timescales for radiation belt electron acceleration and loss due ot resonant wave-particle interactions: 1. Theory, J. Geophys. Res., 112, A04206, doi:10.1029/2006JA011801, 2007a.

Summers, D., N. Binbin, and N. P. Meredith, Timescales for radiation belt electron acceleration and loss due ot resonant wave-particle interactions: 2. Evaluation for VLF chorus, ELF hiss, and electromagnetic ion cyclotron waves, J. Geophys. Res., 112, A04207, doi:10.1029/2006JA011993, 2007b.

Thomsen, M. F., Why Kp is such a good measure of magnetospheric convection, Space Weather, 2, S11044, doi.1029/2004SW000089, 2004.

Thomsen, M. F., M. H. Denton, B. Lavraud, and M. Bodeau, Statistics of plasma fluxes at geosynchronous orbit over more than a full solar cycle, Space Weather, 5, S03004, doi:10.1029/2006SW000257, 2007.

Thomsen, M. F., J. E. Borovsky, R. M. Skoug and C. W. Smith, Delivery of cold, dense plasma sheet material into the near-Earth region, J. Geophys. Res., 108(A4), 1151, doi: 10.1029/2002JA009544, 2003.

Thomsen, M. F., E. Noveroske, J. E. Borovsky and D. J. McComas, Calculation of moments from measurements by the Los Alamos magnetospheric plasma analyzer, LA Rep. LA-13566-MS, Los Alamos Natl. Lab., Los Alamos, NM 87545, 1999.

Tsurutani, B. T., W. D. Gonzalez, A. L. C. Gonzalez, F. L. Guarnieri, N. Gopalswamy, M. Grande, Y. Kamide, Y. Kasahara, G. Lu, I. Mann, R. L. McPherron, F. Søraas and V. Vasyliunas, Corotating solar wind streams and recurrent geomagnetic activity: a review, J. Geophys. Res., 111, A07S01, doi:10.1029/2005JA011273, 2006.

Turner, N. E., E. J. Mitchell, D. J. Knipp and B. A. Emery, Energetics of magnetic storms driven by corotating interaction regions: a study of geoeffectiveness, in Recurrent Magnetic Storms: Corotating Solar Wind Streams, B. T. Tsurutani, R. L. McPherron, W. D. Gonzalez, G. Lu, J. H. A. Sobral and N. Gopalswamy (eds.), pg l.113, AGU, 2006.

Wilken, B., Q.-G. Zong, G. D. Reeves, T. Doke, and T. Yamamoto, Geoactivity in response to CIR/CME events: A synoptic view, Phys. Chem. Earth, 24, 113-117, 1999.

Wrenn, G. L., Chronology of 'killer' electrons: Solar cycles 22 and 23, J. Atmos. Sol-Terr. Phys., (in press) 2009.

Zaharia, S., M. F. Thomsen, J. Birn, and M. H. Denton, Effect of storm-time plasma pressure on the magnetic field in the inner magnetosphere, Geophys. Res. Lett., 32, L03102, doi:10.1029/2004GL021491, 2005.

Zhang, J., M. W. Liemohn, M. F. Thomsen, J. U. Kozyra, M. H. Denton and J. E. Borovsky, A statistical comparison of hot-ion properties at geosynchronous orbit during intense and moderate geomagnetic storms at solar maximum and minimum, J. Geophys. Res., 111, A07206, doi:10.1029/2005JA011559, 2006.

Table 1. Overview of the evolution of the outer electron radiation belt at geosynchronous orbit during a high-speed-stream-driven storm.

Phase of Storm	**Number Density (n)**	**Temperature (T)**	**Pressure (P)**	**Relativistic flux ($\mathcal{F}$)**
Calm before the storm	decreases slowly	constant	decreases slowly	decreases slowly
Relativistic-electron dropout at storm onset	decreases suddenly	???	decreases suddenly	decreases suddenly
Recovery from relativistic-electrion dropout	increases suddenly	???	increases suddenly	increases less suddenly
Long-duration storm	constant	increases slowly	increases slowly	increases slowly

Table 2. Overview of the evolution of the outer electron radiation belt at geosynchronous orbit during a CME-driven storm.

Trigger	**Phase of Storm**	**Number Density (n)**	**Temperature (T)**	**Pressure (P)**	**Relativistic flux ($\mathcal{F}$)**
SSC	Compression of magnetosphere	decreases greatly	decreases slightly	decreases greatly	decreases greatly
South IMF Sheath	Sheath driving	decreases	decreases	decreases	decreases
South IMF Cloud	Cloud driving	increases	decreases	increases	holds steady
Minimum Dst	Recovery	increases	increases	increases	increases

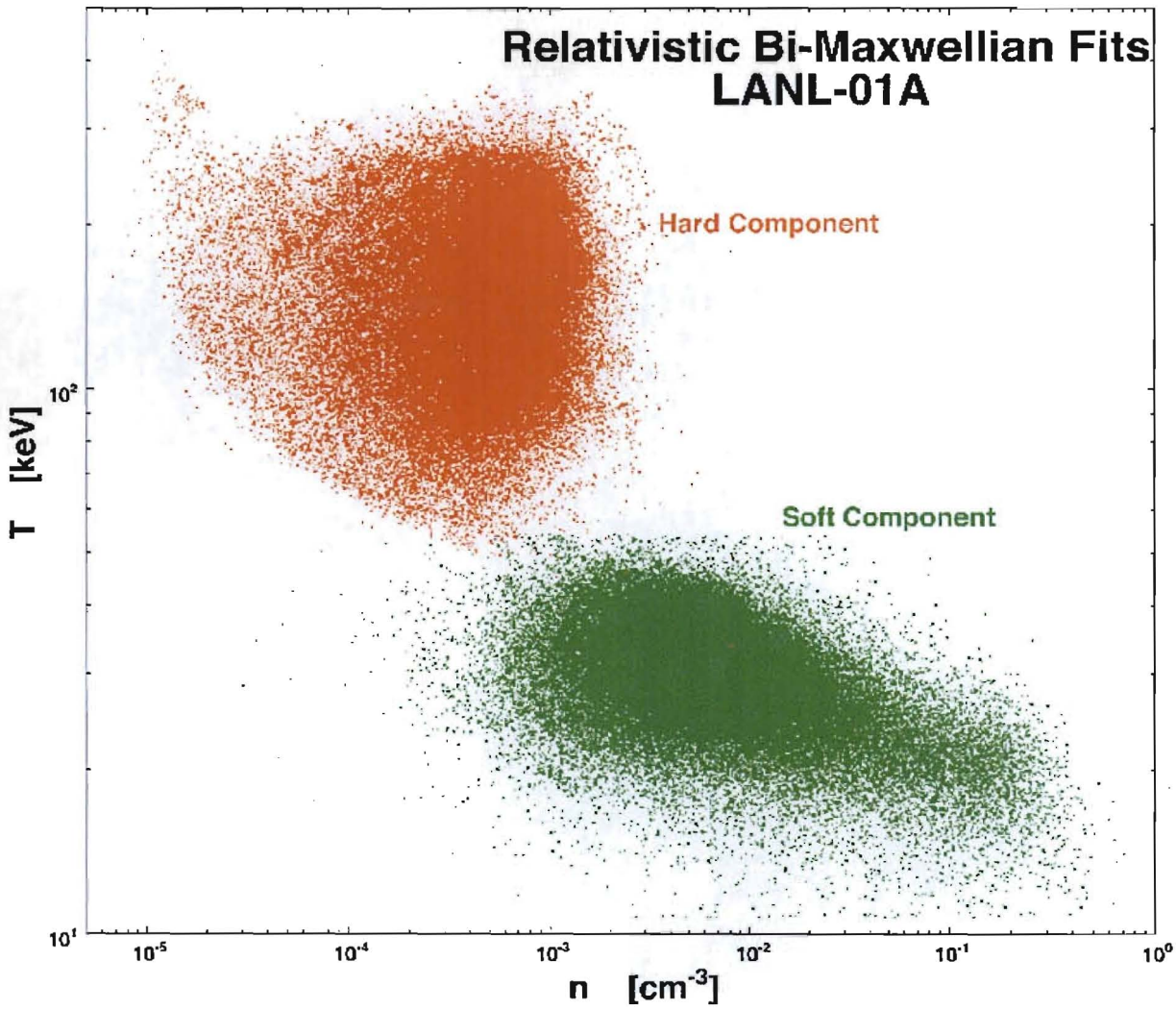

Figure 1. This scatter plot contains half-hour median values of number density and temperature for the spacecraft LANL-01a for the seven years 2001-2007, calculated from two-component relativistic Maxwellian fits. The energetic electrons at geosynchronous orbit divide into a "hard" component with a number density of ~5×10^{-4} cm^{-3} and a temperature of ~150 keV (red points) and a "soft" component with a number density of ~1×10^{-2} cm^{-3} and a temperature of ~300 keV (green points).

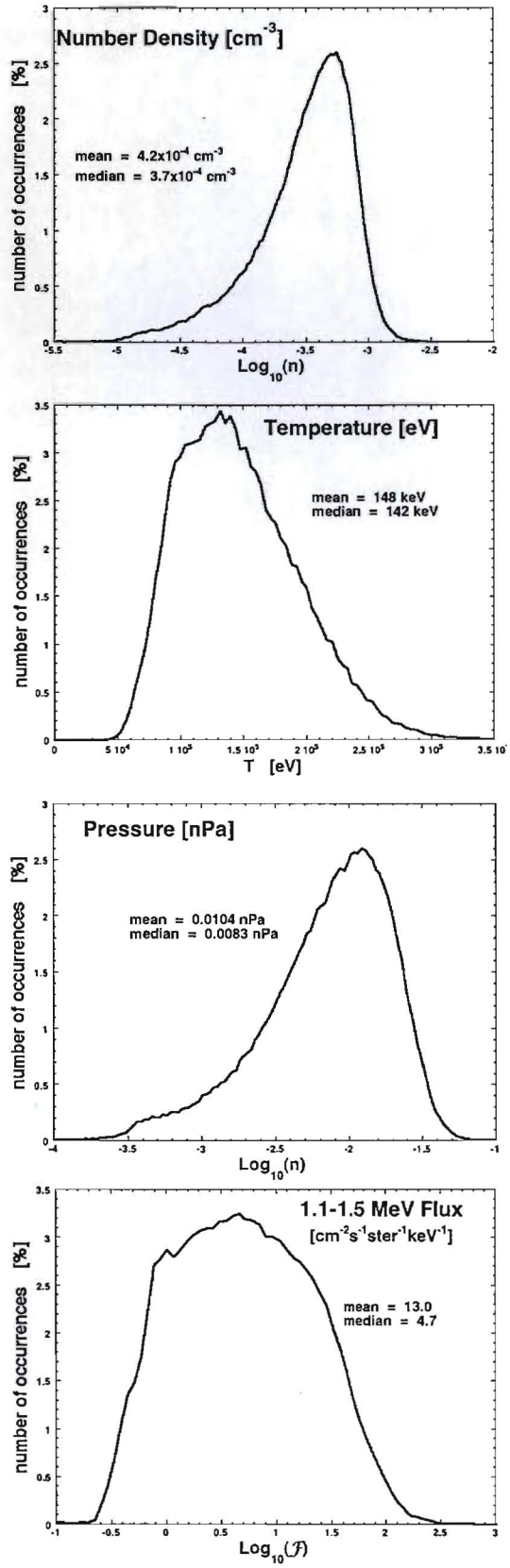

Figure 2. The number density n, temperature T, pressure P = nkBT, and relativistic-electron flux $\mathcal{F}$ of the outer electron radiation belt at geosynchronous orbit are binned to produce occurrence distributions. Note that the base-10 logarithm of n, P, and $\mathcal{F}$ are binned. The first three panels are for 955,527 half-hour measurements from 7 satellites and the bottom panel is for 278,471 half-hour multisatellite averages.

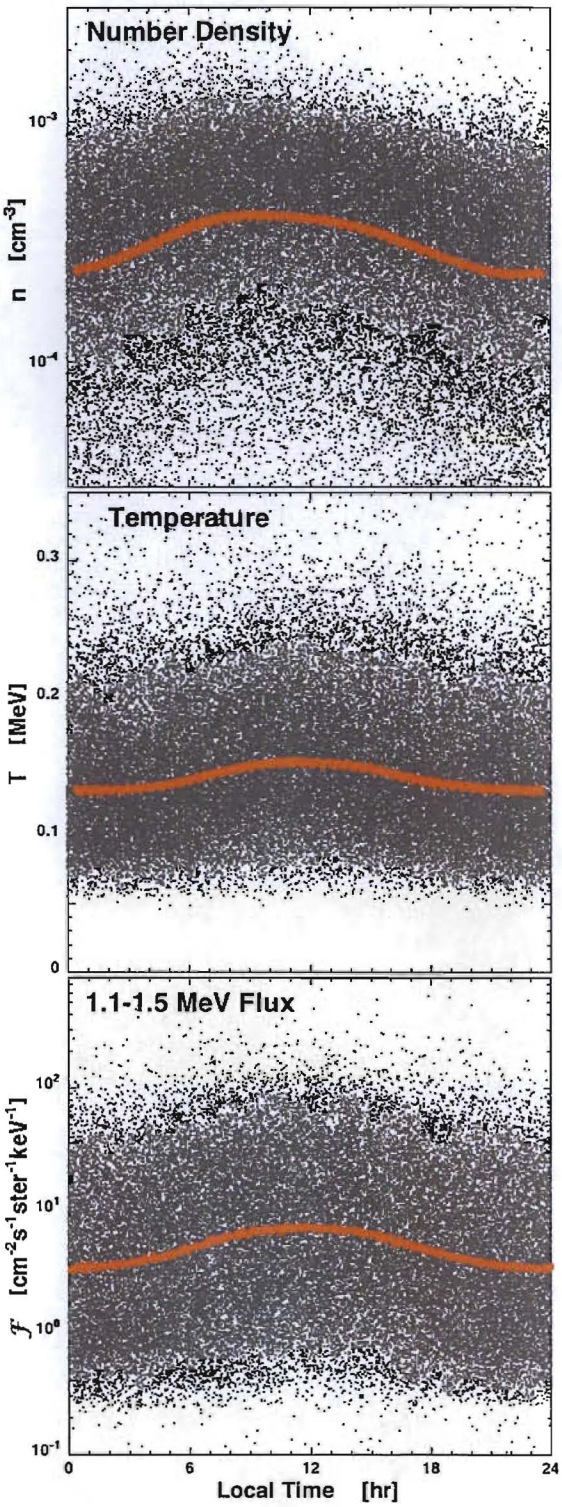

Figure 3. For 955,527 half-hour measurements (1990-2007), the number density (top panel) and temperature (middle panel) are plotted as a function of the local time at which the measurement was obtained. For 876,391 half-hour measurements (1989-2006), the 1.1-1.5 MeV electron flux is plotted as a function of local time. The gray points are the individual measurements and the red points are 3000-point averages of the gray points.

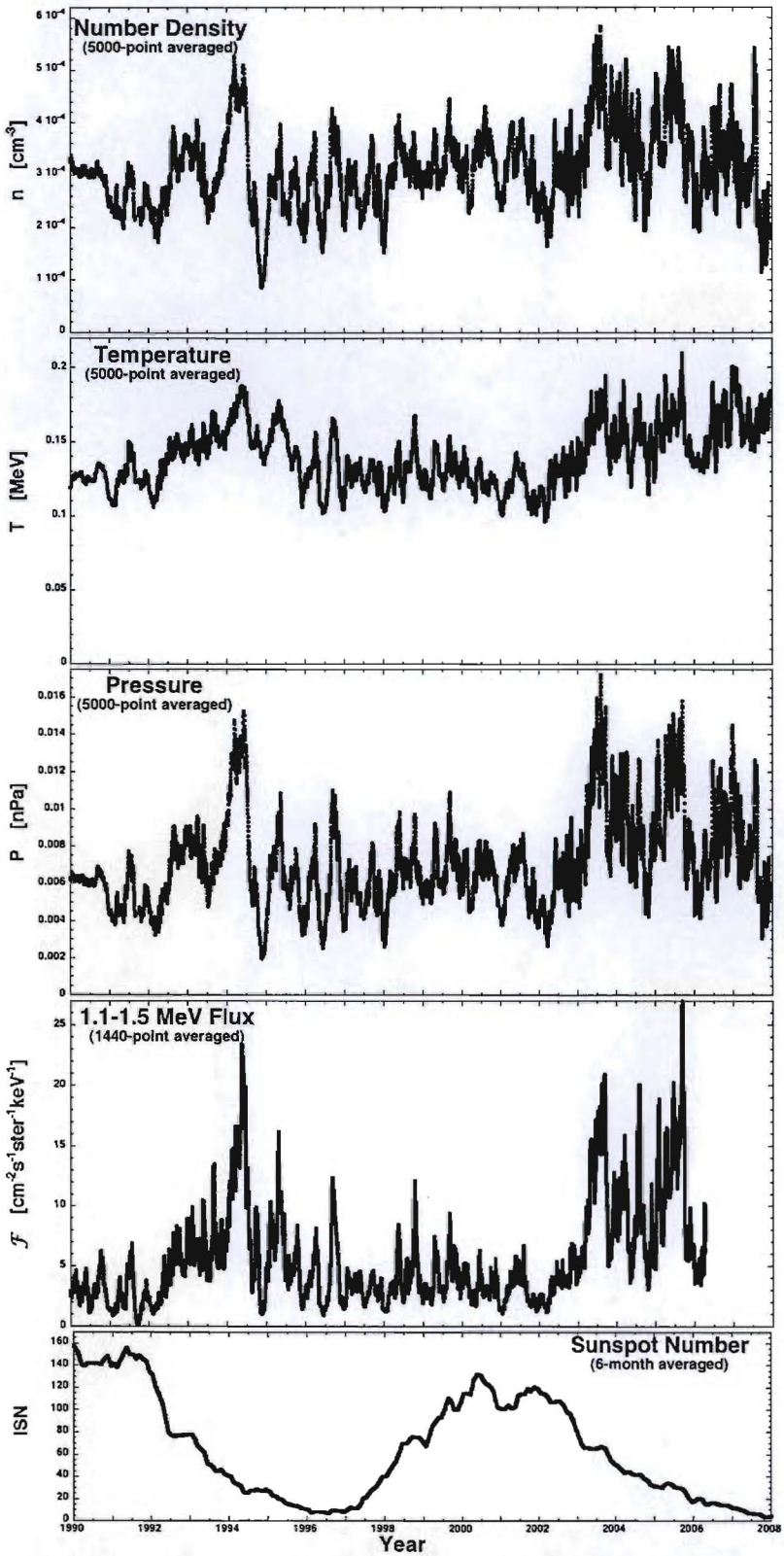

Figure 4. Plots of the number density n (top panel), temperature T (second panel), pressure $P=nk_BT$ (third panel), and 1.1-1.5 MeV flux $\mathcal{F}$ (fourth panel) of the outer electron radiation belt at geosynchronous orbit as a function of time for 18 years. In the top three panels the black points are 5,000-point logarithmic averages of the 955,527 half-hour measurements from 7 satellites; in the fourth panel the black points are 1440-point logarithmic averages of the 278,471 half-hour multisatellite averages. The international sunspot number (ISN) is plotted in the bottom panel.

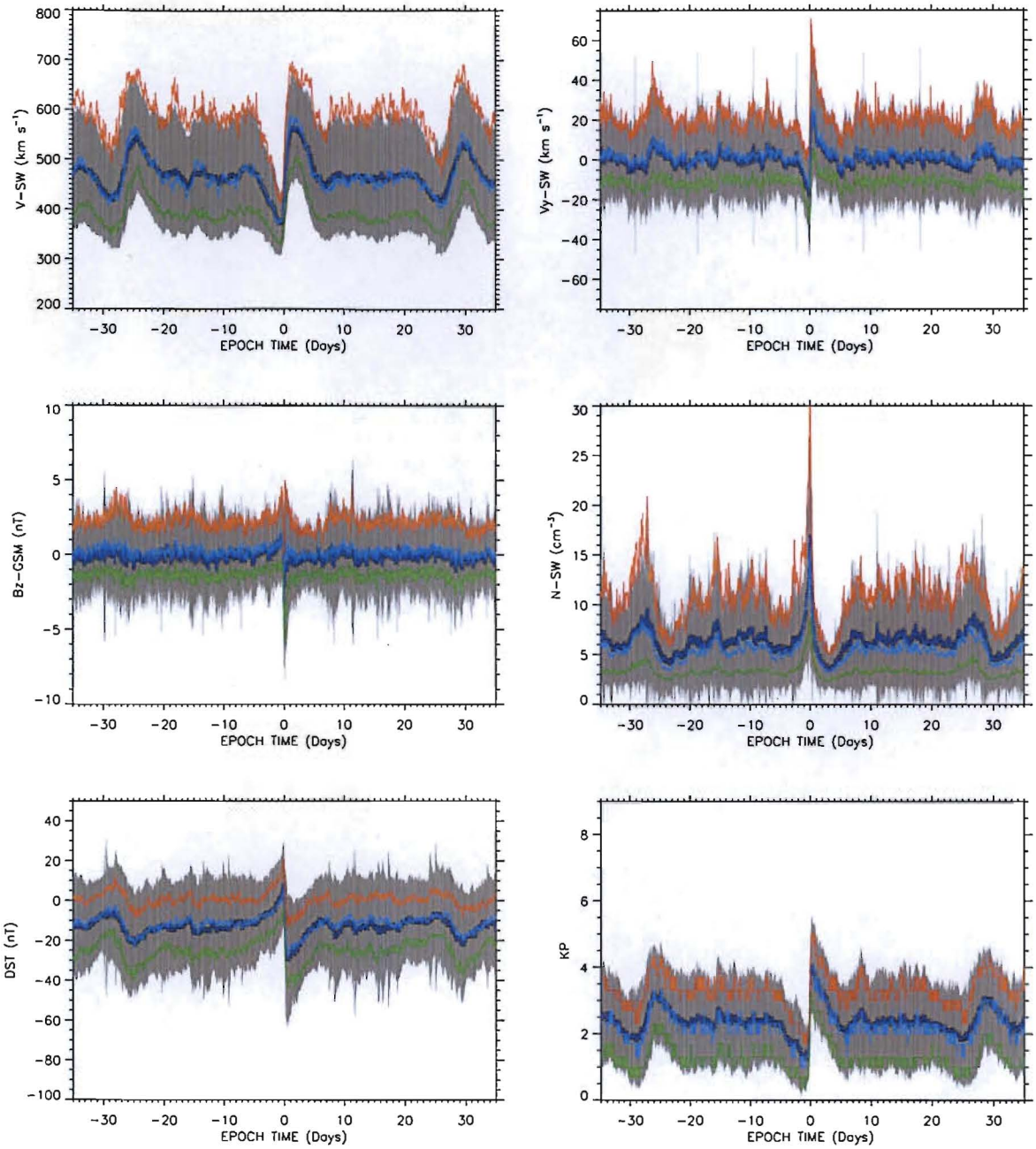

Figure 5. Selected solar wind parameters as a function of epoch time for 124 HSSs between 1993 and 2006. The upper quartiles on the measurements are shown in red whilst the lower quartiles are shown in green. The mean value of each parameter is plotted in dark blue whilst the median is plotted light blue. The grey shaded region indicates values within one standard deviation of the mean.

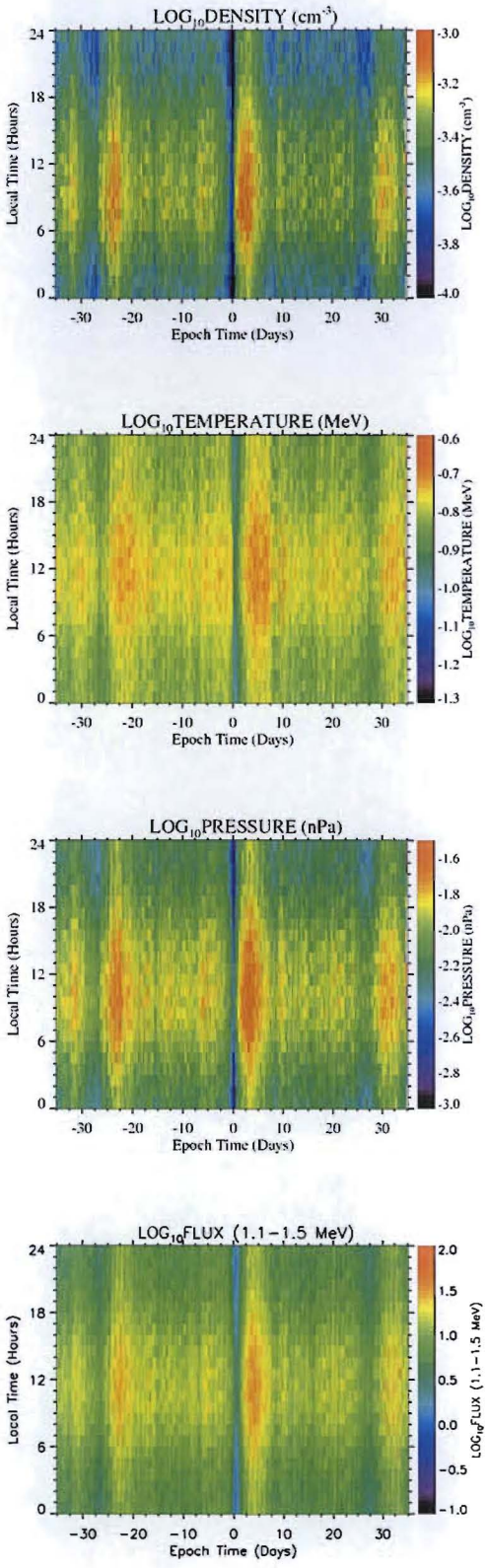

Figure 6. Superposed outer electron radiation belt number density, temperature, pressure, and flux, calaulated using a superposed epoch analysis of 124 high speed solar wind streams between 1993 and 2006. Averaged values of these parameters at one-hour time resolution are displayed for ±35 days from the zero epoch of convection onset.

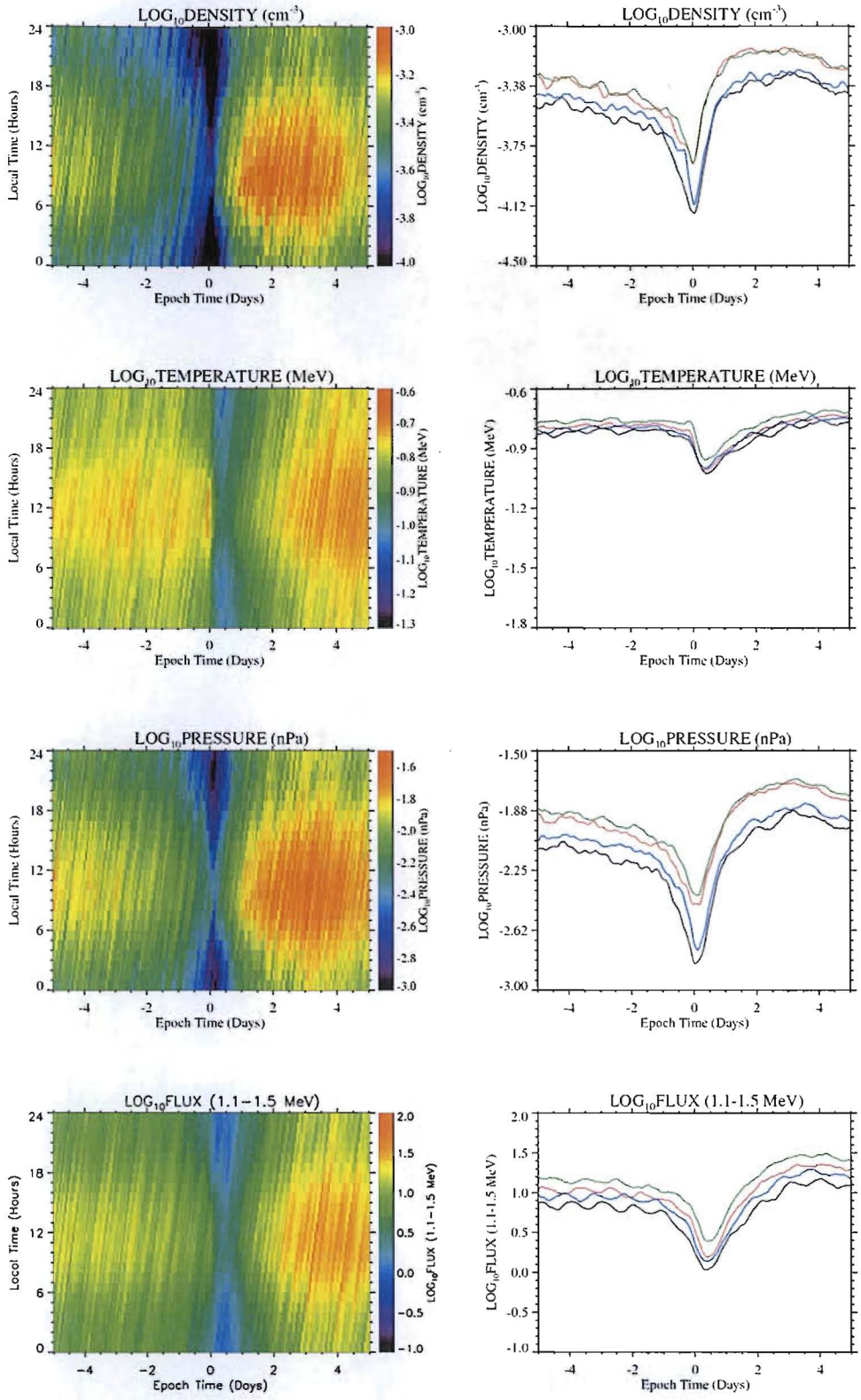

Figure 7. Superposed outer electron radiation belt number density, temperature, pressure, and flux, calaulated using a superposed epoch analysis of 124 high speed solar wind streams between 1993 and 2006. Averaged values of these parameters at one-hour time resolution are displayed for ±5 days from the zero epoch of convection onset. The left-hand column contains enlarged versions of the data from Figure 6. In addition, the number density, temperature, pressure, and flux are averaged over 3-hour local time bins and plotted as a function of epoch time (23-01 LT (black), 05-07 LT (red), 11-13 LT (green), and 17-19 LT (blue)).

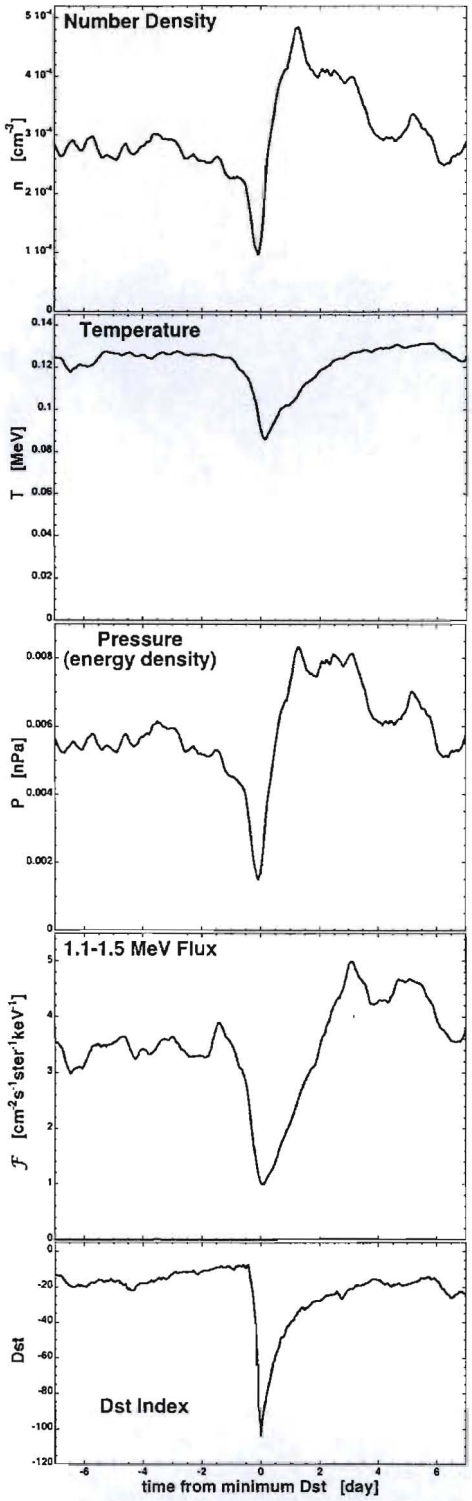

Figure 8. For 78 coronal-mass-ejection-driven storms, superpositions of the number density n, temperature T, and pressure P of the outer electron radiation belt at geosynchronous orbit are plotted as functions of time as is the 1.1-1.5 MeV electron flux and the Dst index. Each curve in the first four panels is a local-time average of the quantity. Time t=0 is taken to be the time of minimum Dst in the storm.

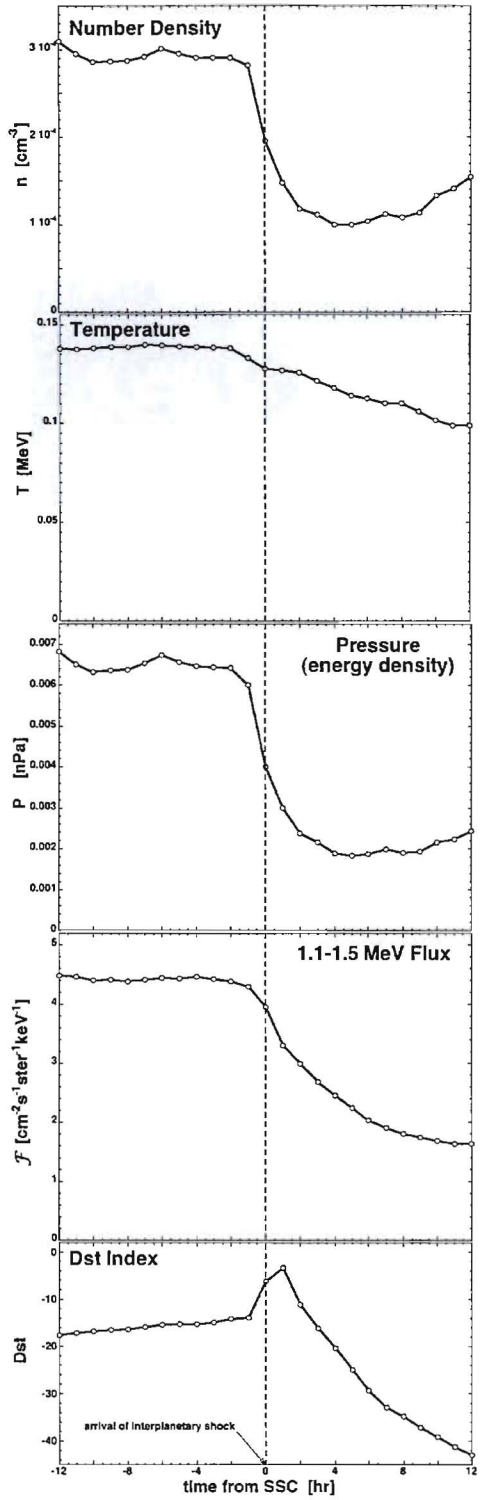

Figure 9. For 535 well-defined SSC (storm sudden commencement) events, superpositions of the number density n, temperature T, and pressure P of the outer electron radiation belt at geosynchronous orbit are plotted as functions of time as is the relativistic-electron flux and the Dst index. Each curve in the first four panels is a local-time average of the quantity. Time t=0 is taken to be the time of SSC (arrival at Earth of an interplanetary shock).

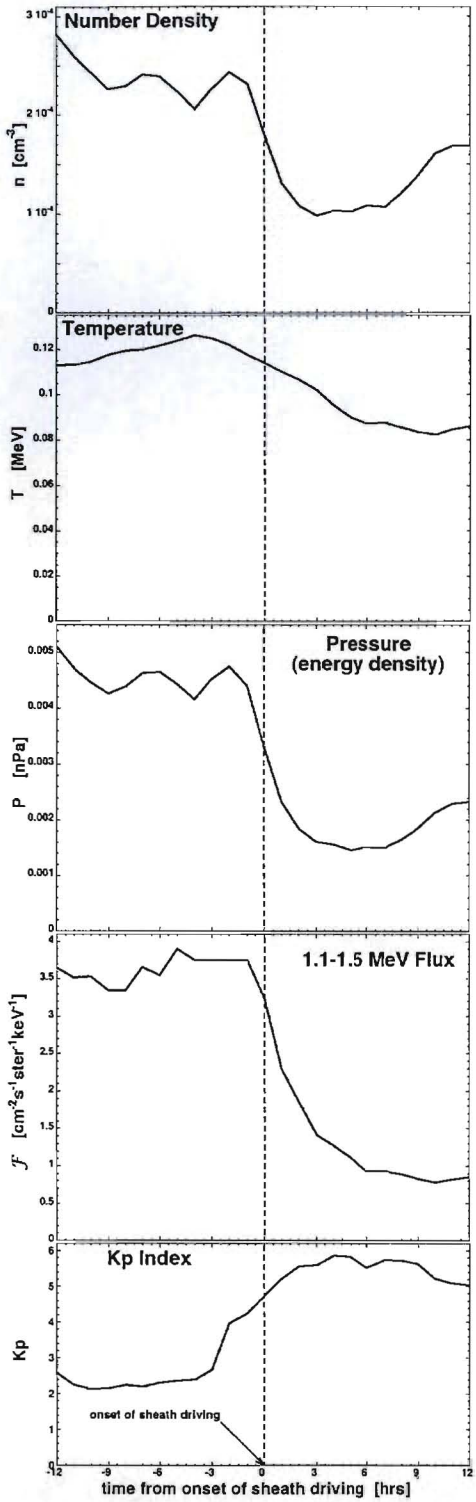

Figure 10. For 16 cloud-driven storm events with well-defined intervals of southward IMF (GSM) in the CME sheaths, superpositions of the number density n, temperature T, and pressure P of the outer electron radiation belt at geosynchronous orbit are plotted as functions of time as is the relativistic-electron flux and the Kp index. Each curve in the first four panls is a local-time average of the quantity. Time t=0 is taken to be the onset of the southward-IMF interval in the sheath plasma.

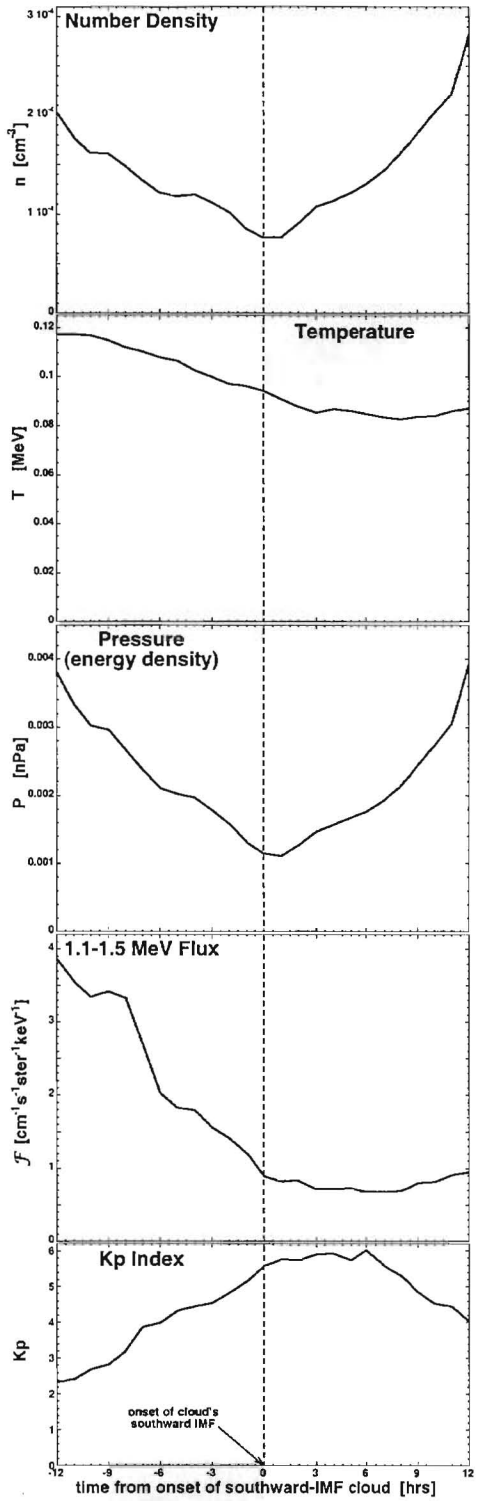

Figure 11. For 13 magnetic clouds with well-defined southward-IMF (GSM) portions, superpositions of the number density n, temperature T, and pressure P of the outer electron radiation belt at geosynchronous orbit are plotted as functions of time. Each curve is a local-time average of the quantity. Time t=0 is taken to be the onset of the southward-IMF portion of the clouds.

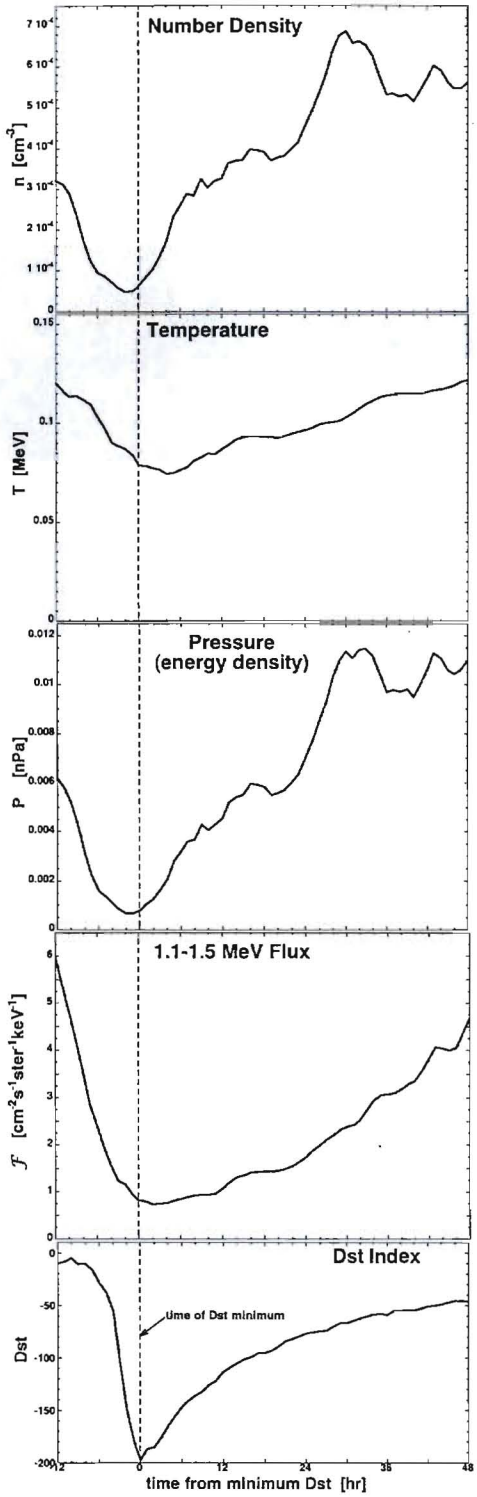

Figure 12. For 17 magnetic-cloud-driven storms with strong, single-dip Dst perturbations, superpositions of the number density n, temperature T, and pressure P of the outer electron radiation belt at geosynchronous orbit are plotted as functions of time, as is the superposition of the relativisitic-electron flux and the Dst values. Each curve in the first four panels is a local-time average of the quantity. Time t=0 is taken to be the time of minimum Dst.